ELSEVIER

MISR-based passive optical bathymetry from orbit with few-cm level of accuracy on the Salar de Uyuni, Bolivia

Bruce G. Bills [a,b,*], Adrian A. Borsa [b], Robert L. Comstock [b]

[a] *NASA Goddard Space Flight Center, Greenbelt, MD, United States*
[b] *Scripps Institution of Oceanography, La Jolla, CA, United States*

Abstract

We demonstrate that, under ideal circumstances, passive optical measurements can yield surface water depth estimates with an accuracy of a few centimeters. Our target area is the Salar de Uyuni, in Bolivia. It is a large, active salt flat or playa, which is maintained as an almost perfectly level and highly reflective surface by annual flooding, to a mean depth of 30–50 cm. We use MISR data to estimate spatial and temporal variations in water depth during the waning portion of the 2001 flooding cycle. We use a single ICESat laser altimetry profile to calibrate our water depth model. Though the salt surface is probably the smoothest surface of its size on Earth, with less that 30 cm RMS height variations over an area of nearly 10^4 km^2, it is not completely featureless. Topography there includes a peripheral depression, or moat, around the edge of the salt, and several sets of prominent parallel ridges, with 5 km wavelength and 30 cm amplitude. The process by which these features form is still not well characterized.
© 2006 Elsevier Inc. All rights reserved.

1. Introduction

The Salar de Uyuni is a large salt flat on the Altiplano of Bolivia, whose surface is maintained in an almost perfectly flat, smooth, and level configuration by annual flooding during the rainy season. The objective of the present investigation is to use the known optical absorption and reflection properties of water to estimate the spatial and temporal variations in the depth of water covering the salt surface, and from that to deduce the salt surface topography. We present a general description of the field area, describing the features which make it an almost ideal laboratory for passive optical determination of shallow water depth variations, and the scientific interest in study of the salt surface topography. We also present a brief description of the algorithm used to determine water depth from passive satellite optical observations, with some discussion of relevant approximations and possible error sources. We compare the results obtained with

two independent estimates of the salt surface topography. One of them is from a satellite laser altimeter on ICESat, which yields profiles along the sub-satellite track. The other is from a GPS survey of a region of the salar surface which was conducted as part of an ICESat calibration and validation activity.

The basic concept behind our measurement strategy is very simple. Water absorbs light, with a relatively strong dependence on wavelength. Red light is more strongly absorbed than blue light, which explains the common observation that, for example, the light which is returned after reflection from the bottom of a white swimming pool has a bluish appearance. The effect is more pronounced in deeper water and can be used to determine the depth of a shallow water body, but only if the amount of reflection from the bottom is well understood. We report on an application of this principle, in nearly ideal circumstances.

This basic approach to estimating shallow water depths using the absorption of light, is not new (Clark, 1987; Lee et al., 1998, 1999; Lyzenga, 1978; Philpot, 1989). It has been widely applied in a variety of different environments (Adler-Golden et al., 2005; Fonstad & Marcus, 2005; Isoun et al., 2003; Lafon et al., 2002; Mobley et al., 2005; Sandidge & Holyer, 1998). This

application is quite distinct from passive optical estimates of the areal extent of shallow water bodies (Bryant, 1999; Castaneda et al., 2005) and from laser measurements of water depth (Guenther et al., 2000; Finkl et al., 2005; Wozencraft & Lillycrop, 2003).

A frequently encountered difficulty in passive optical bathymetric applications is the determination of the reflective properties of the bottom surface (Bierwirth et al., 1993; Stumpf et al., 2003), which in many applications is quite spatially variable and not directly accessible. Our application is very simple in that regard, since the bottom of the water column is a very nearly homogeneous, smooth, and highly reflective salt layer (Lamparelli et al., 2003; Ponzoni et al., 2004). In addition, we have access to the salt surface during times of the year when the water layer is absent. We can thus easily measure the reflective properties of the dry substrate, and use that to estimate its behavior when wet. This removes an important source of error in other similar applications.

A number of satellites routinely provide data from which analyses of the type we present here could be performed. A partial list would include LandSat, MODIS (Moderate Resolution Imaging Spectroradiometer), ASTER (Advanced Spaceborne Thermal Emission and Reflection Radiometer), and MISR (Multiangle Imaging SpectroRadiometer). Each of them has advantages and disadvantages. The two with highest spatial resolution (LandSat and Aster) provide irregular temporal coverage. MODIS provides the best temporal coverage, often with two images per day.

Our choice of MISR as data source was initially motivated by three considerations: regular temporal sampling (16 day repeat interval), multiple spectral bands (blue, green, red, and infrared), and multiple viewing angles (one nadir pointed, and 8 off-nadir, with 4 forward and 4 backward). This allows 5 different path lengths through the water column at each location on each pass. In clear water this would provide an over-determined solution for the absorption depth, and in turbid water would allow for modeling and removal of sedimentary influences. It would also allow characterization of the bottom reflectance and in-path absorption from a single pass of data. Despite these advantages, the analysis presented here uses only the nadir data. However, we also benefited from the considerable ancillary data provided by the MISR project, including the incident radiation in each spectral band, at each pixel location.

In most previous applications, a challenge has been to extend the depth range of the method, and thereby reach the bottom over as large an area as is possible. For that purpose, blue or green light is frequently used. In our application, we have almost the exact opposite problem. The water is very shallow, and in the green and blue spectral range, the absorption is minimal. We thus mainly exploit the red and infrared channels. However, for consistency checks, we have used all 4 spectral bands of MISR.

Our analysis shows that the salt surface is very flat and smooth, but not completely without topographic relief. Visual inspection of the surface shows that it is quite rough at millimeter scale, and there is a wide-spread pattern of polygonal cracks with typical spacing of 1–2 m, but very little associated relief. Standing on the surface, one has the impression that it is perfectly level and smooth at scales beyond a meter. That impression is almost, but not quite, correct. There are several types of topographic features on the salt. The largest is a peripheral trough or moat, extending almost continuously around the edge of the salar, with a typical width of 1–3 km, and a depth of 20–50 cm. In addition, there are several sets of oriented, quasi-sinusoidal ridges, with wavelengths of 5 km and amplitudes of 20–30 cm. These features are best developed on the western portion of the salar.

The remainder of this paper is organized into 5 sections. In Section 2 we give a summary of the geographic background of the Salar de Uyuni. In Section 3 we briefly describe the algorithm used to estimate water depth. In Section 4 we describe the data used and application of the algorithm. In Section 5 we present the results of our analysis. In Section 6 we present a brief summary and conclusion.

2. Geographic background

As will be shown below, the Salar de Uyuni has an extraordinarily flat, level, and smooth surface, but it is not completely devoid of surface relief. The geomorphic processes which produce and maintain the essentially flat surface are reasonably well understood (Rosen, 1994; Yechieli & Wood, 2002), but those which produce the minor relief are as yet not well characterized. Indeed, the very existence of surface features with amplitudes of decimeters and wavelengths of kilometers has not,
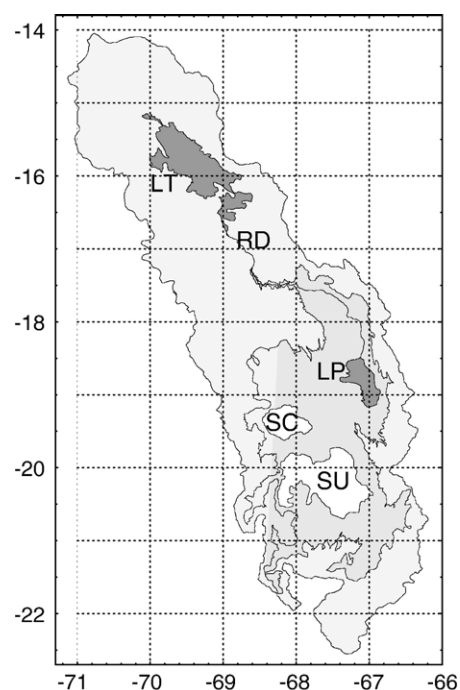

Fig. 1. Location map. The Salar de Uyuni occupies the lowest sub-basin of the central Altiplano. The light shading indicates the drainage basin of paleolake Minchin. Darker shading indicates the outline of Lake Minchin at its highest level. Other features are Lake Titicaca (LT), Lake Poopo (LP), rio Desaguadero (RD), salar de Coipasa (SC), and Salar de Uyuni (SU).

to our knowledge, otherwise been recognized. With the exception of a few rocky "islands" which protrude through the salt surface, the Salar de Uyuni has less than 1 m of relief over an area of nearly 10^4 km², and there is a 50 * 50 km region in the northeastern sector which is completely devoid of visible topography. We believe that the Salar de Uyuni is the flattest surface of its size on Earth. Even ignoring wind waves, most parts of the ocean surface depart from an exact equipotential surface by decimeters due to the effects of currents (Nerem, 1990). To put this peculiar surface in context, we now briefly describe its environment and background.

The Altiplano of Bolivia is a cold high desert, but at elevations below 3800 m the landscape is dominated by coastal geomorphic features. During colder and/or wetter episodes in the past, the hydrologically closed basins of the Altiplano have contained substantial lakes. This region contains several hemiarid lake basins (Currey, 1994a,b), characterized by dual hydroclimates; the non-arid highlands exhibit a net positive annual water balance, while the arid lowlands have a negative balance. The Salar de Uyuni forms the flat floor of the lowest such basin in the southern Altiplano. Fig. 1 illustrates the location of the Salar de Uyuni, and other features of note.

Lake Titicaca occupies the lowest part of the northern portion of the closed drainage area of the Central Andes. Over the past century Lake Titicaca has stood at an elevation close to 3810 m and has exported water to the south, through the Rio Desaguadero outlet, for at least part of nearly every year (Roche et al., 1992). The amount of water exported per year varies considerably and is well correlated with the El Nino–Southern Oscillation cycle (Garreaud & Aceituno, 2001; Lenters & Cook, 1997, 1999). The lake level has exhibited pronounced variations over the Holocene and Late Pleistocene (Abbott et al., 1997; Cross et al., 2000; Rowe & Dunbar, 2004) in response to climatic changes.

The much larger southern basin, into which Titicaca exports water, presently contains only one perennial lake, Lake Poopo

Table 1
MISR spectral bands

Band	Center wavelength (nm)	Band width (nm)	Absorption length HQ73 (m)	Absorption length PF97 (m)
Blue	446.34	40.89	33.0 ± 7.2	146 ± 55
Green	557.54	27.17	19.4 ± 6.8	16.7 ± 3.7
Red	671.75	20.44	2.67 ± 0.39	2.28 ± 0.24
Infrared	866.51	38.62	0.214 ± 0.054	

(3686 m elevation, 3–4 10^3 km² area), and the large playas of Empexa, Coipasa, and Uyuni. The early work of Agassiz (1876), Minchin (1882), Steinmann et al. (1904) and Bowman (1909) established that a series of large lakes have, at various times throughout the Pleistocene, occupied this basin. A calcium carbonate tufa layer covers much of the landscape below 3760 m, and is particularly conspicuous near 3720 m (Minchin, 1882; Rouchy et al., 1996). It was deposited whenever the water became locally saturated with carbonate (Ford & Pedley, 1996). Similar tufa features are found in association with paleo-lakes Lahontan (Benson, 1994) and Bonneville (Felton et al., 2006; Hart et al., 2004; Nelson et al., 2005), both in the Great Basin of western United States. Steinmann et al. (1904) called the Altiplano lake stand at this level Lake Minchin, since Minchin (1882) had described "a white and perfectly horizontal line running around certain spurs of the Oruro hills...at a height of 200 feet above the present level of Lake Poopo".

Servant and Fontes (1978) provided the first radiocarbon dates on shorelines of Lake Minchin and suggested that the highest stand of the lake (at close to 3800 m) occurred prior to 28 ky ago. They also identified a separate episode of pluvial activity, which they called the Tauca stage, and suggested that it culminated near 3720 m elevation at about 12 ky BP. By defining the Tauca stage to be both lower and younger than the Minchin stage, Servant and Fontes (1978) set up the possibility of a nomenclature conflict, which has in fact emerged. Subsequent work has significantly clarified the timing of Late Pleistocene lake level variations on the Altiplano (Argollo & Mourguiart, 2000; Baker et al., 2001a,b; Baucom & Rigsby,
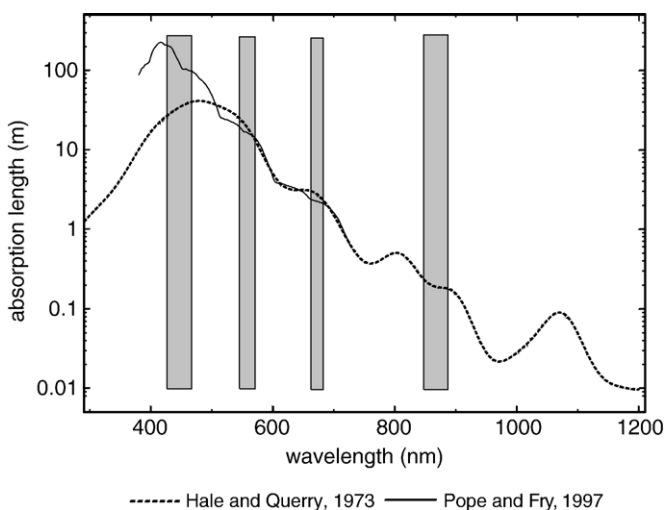

Fig. 2. Water absorption spectrum. The absorption length, or reciprocal of the absorption coefficient, is plotted against wavelength over the visible and near infra-red part of the spectrum. Data are from Hale and Querry (1973) and Pope and Fry (1997). Also shown are the MISR optical bands.
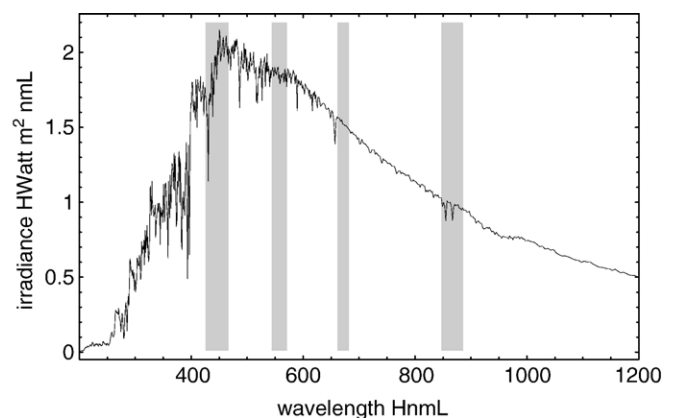

Fig. 3. Solar irradiance spectrum. The solar irradiance (Watt/m²/nm) above the atmosphere is shown from the compilation of Wehrli (1985). Also shown are the MISR optical bands.

1999; Chepstow-Lusty et al., 2005; Fornari et al., 2001; Placzek et al., 2006). It is now known that the highest Late Pleistocene stand of the lake was roughly coincident with the timing ascribed by Servant and Fontes (1978) to their Tauca stage, but at an elevation equal to, and even briefly above (Bills et al., 1994), the nominal Minchin stage. We will use the term Lake Minchin to refer to the late Pleistocene lake.

The Salar de Uyuni contains most of the salt which was in solution in Lake Minchin. Most of the remainder is in the

A   MISR image 19 April 2001
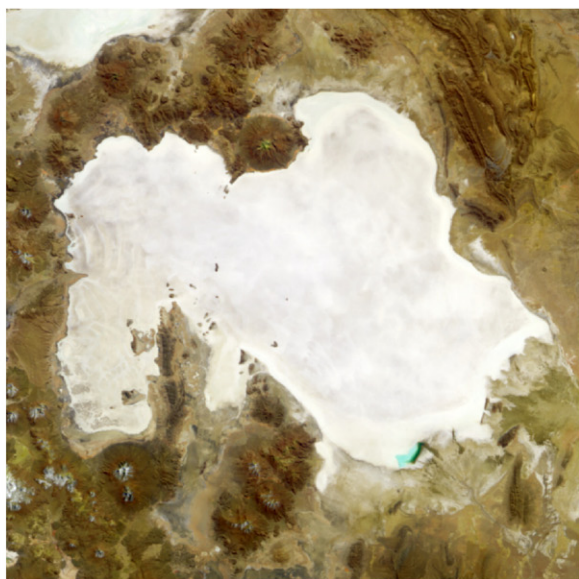

B   MISR image 18 November 2003

Fig. 4. Study area at wet and dry times: A) MISR image of study area, acquired on 3 April 2001, when water covered the Salar de Uyuni. B) MISR image of same area, on 18 October 2003, a time when the salt was dry. Note that dry salt is much brighter than the surrounding area, and wet salt is substantially darker. Note also the variations in water depth, visible as various shades of blue in the wet image. (For interpretation of the references to colour in this figure legend, the reader is referred to the web version of this article.)
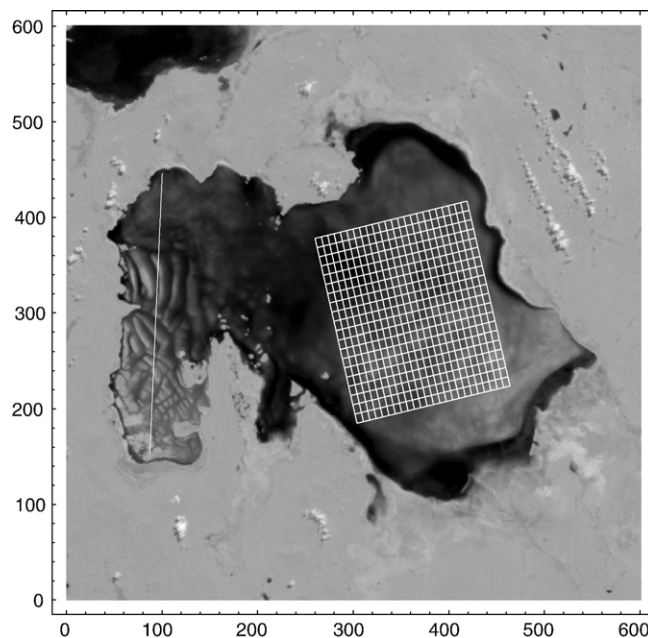

Fig. 5. Location of GPS survey grid and ICESat profile. The rectangular grid is the location of the GPS survey. The isolated white line indicates location of ICESat track number 1320. Background is derived water depth.

adjacent salars of Coipasa, to the north, and Empexa, to the west. The surface crust at Uyuni is almost pure halite (Rettig et al., 1980; Risacher & Fritz, 1991a,b) that is 5 m thick, on average, and attains a peak thickness in excess of 10 m near the eastern margin. There are trace amounts of lithium, bromine, and other elements in the brine which saturates the sub-surface (Risacher & Fritzet, 2000). Beneath the surface salt crust is a sequence of alternating layers of lacustrine silt, and dense crystalline salt, deposited during earlier lake cycles. Two separate drilling operations, in very nearly the same location (Baker et al., 2001a; Fornari et al., 2001), have penetrated these layers to depths below 100 m.

The process of salt deposition from the lake is relevant to an understanding of the present salt crust morphology. As the lake level began to fall under climatic influence, the salinity level began to increase and saturation was reached at an elevation estimated to be 3670 m (Risacher & Fritzet, 2000), or almost 20 m above the present salar surface. At that point, halite would begin to precipitate out of the water column, onto the lake bed. The lake water would remain essentially at the halite saturation point and, with further evaporative loss, would increase its concentration in other dissolved minerals, until they too reached saturation and began to precipitate. If the decline in water level was monotonic, by time the water was completely gone, the accumulated depth of halite and other salts would increase down the slopes to a nearly constant value at the flat basin floor, and the concentration of the bittern salts (mainly bromides, borates, and sulfates) would increase, relative to halite, down toward the bottom. The present situation differs from that scenario in that essentially all of the salts which were deposited on the surrounding slopes have been subsequently transported onto the flat basin floor. An estimate of the amount of post-depositional transport comes from the observations of a

bromine peak at roughly 30 cm depth below the present salt crust (Risacher & Fritzet, 2000). The inference is that all of the salt above that depth was initially deposited up-slope and has been reworked basinward.

As the lake level stabilized at various elevations, either due to climatic stability or temporary overflow into adjacent sub-basins, shorelines were formed as horizontal markers on the landscape. The load associated with Lake Minchin was sufficient to depress the crust and upper mantle by roughly 30 m (Bills et al., 1994). Since removal of the load, the surface has rebounded, and the shorelines are found at higher elevations on mountains which were islands in the middle of the lake than on the periphery. This rebound process, if unopposed, would have produced roughly 10 m of relief on the Salar de Uyuni surface. In addition, there are at least two north–south oriented faults, with significant offset north and south of the salar, that are evident in gravity data across the salar (Cady & Wise, 1992) and would be expected to generate surface relief. However, neither of these de-leveling processes has been able to overcome the action of annual flooding and salt redeposition. In this regard, it is similar to behavior recently documented in the Salar de Atacama (Jordan et al., 2002).

There are numerous other salars in Northern Chile (Risacher et al., 2003; Stoertz & Ericksen, 1974). Many of them are no longer active. In those cases, though there may be thick

accumulations of salt, the surface is not maintained in the same smooth and level form as during deposition from shallow water bodies. The Salar de Atacama is a prime example. It has a surface salt layer several hundred meters thick (Lowenstein et al., 2003), but the last episode of active surface deposition was between 3500 and 5000 years ago (Bobst et al., 2001). Since that time the surface of the salt has become quite rough, at the meter scale (Kempf & Tyler, 2006). In contrast to that situation, the annual flooding of the Salar de Uyuni keeps it much smoother. It appears that surfaces as flat and smooth as that seen at Uyuni must be actively maintained.

3. Algorithmic development

In this section we briefly describe the algorithm used to estimate water depth variations. The observations are of the brightness, or intensity, of light reflected from the Earth's surface in a given direction, location, and wavelength band. The brightness values obtained when the surface is covered with water are less than if the observations were made of the same location at a time when the surface was free of water. We need to develop the relationship between the observed brightness at a given location, and the reflective and absorptive losses which occur, in order to use the optical measurements to estimate
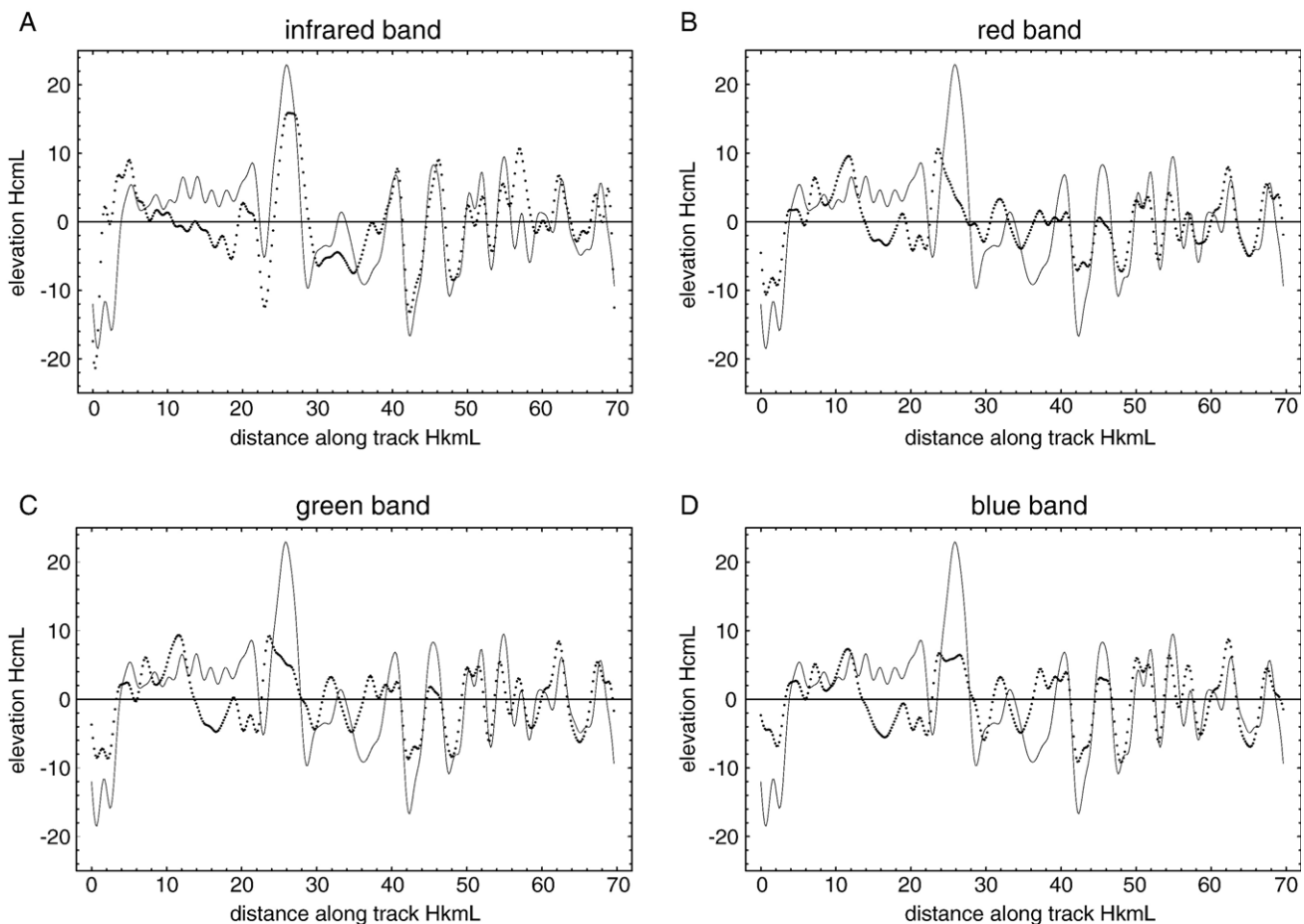

Fig. 6. Along-track comparisons of ICESat-derived and MISR-derived elevation estimates. A) Infrared band, B) red band, C) green band, D) blue band.

water depth. We first describe the general principles governing the absorption and reflection of light and then adapt them to the geometry of our water depth estimation problem.

The Beer–Lambert law of optical absorption (Gordon, 1989; Gordon et al., 1975; Sokoletsky, 2005) states that the rate of absorption along an optical path depends linearly on the concentration of the absorbate. This results in attenuation which is exponential along the path, with an absorption coefficient which depends on wavelength and composition of the material. Fig. 2 illustrates the absorption spectrum of pure water (Hale & Querry, 1973; Pope & Fry, 1997). Also shown in that figure are the spectral pass bands for the MISR instrument. The quantity plotted in the figure is an absorption length scale, given by the reciprocal of the absorption coefficient. It is the depth over

which the incident radiation would be attenuated to $1/e$ of the input value. The effective absorption lengths of pure water in the MISR bands are listed in Table 1. The first estimate is from Hale and Querry (1973), the second from Pope and Fry (1997).

We note that, in most applications of optical absorption properties to water depth estimation, shorter wavelengths are preferred, since they allow greater depth of penetration. We are in the unusual situation of examining sufficiently shallow water that the stronger absorption at longer wavelengths is actually an advantage. The water on the Salar de Uyuni is, in most places, shallow enough that the absorption in the blue is expected to be quite negligible. Thus the significant revision in water absorption length in the blue part of the spectrum, in the more recent compilation, has minimal impact on our work. Though
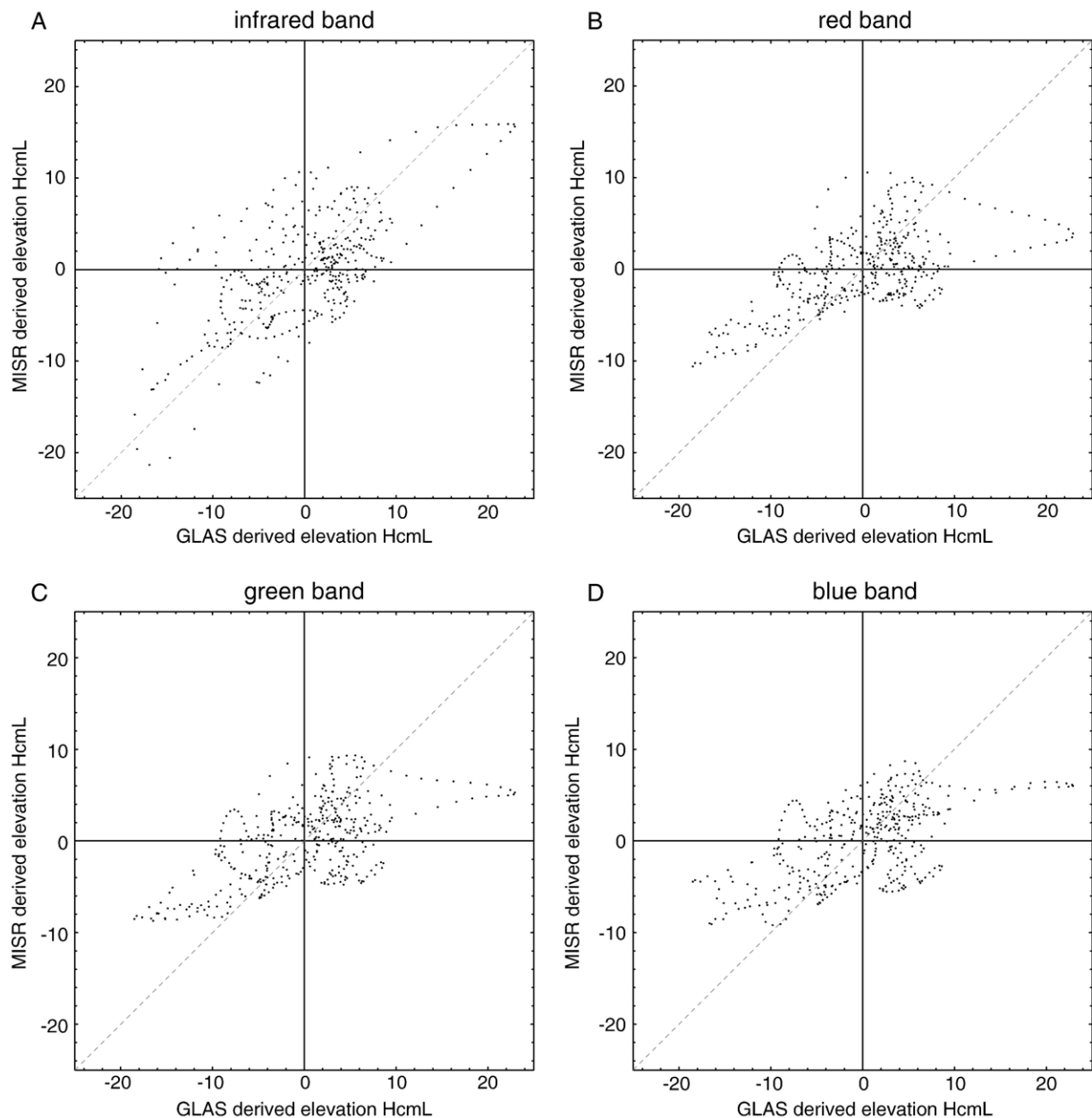

Fig. 7. Scatter-plot comparisons of ICESat-derived and MISR-derived elevation estimates. A) Infrared band, B) red band, C) green band, D) blue band.

the absorption does depend weakly on salinity and temperature (Millard & Seaver, 1990; Smith & Barker, 1981; Yunus, 1992), we will ignore those variations. We also need to know the input spectrum. Fig. 3 shows the solar spectrum from the compilation by Wehrli (1985).

A particular feature of our study area which facilitates this analysis is that we are able to observe the surface in both dry and flooded states. We can thus easily characterize spatial variations in the reflectivity of the salt surface when it is sub-aerially exposed, and then use that as a guide to estimating spatial variations in the reflectivity of that surface when it is covered by water.

The measured intensity of light, as seen by the MISR instruments, when looking at a point on the salt surface, will have multiple contributions. One contribution is a specularly reflected image of the sky. Another contribution is an image of the Sun, attenuated via reflective losses at both the top and bottom of the water column, and absorptive losses within the water column. An expression for the observed brightness can be written as

$$F = b + f\left(\frac{(1-R_1)^2 R_2 q^2}{1 - R_1 R_2 q^2}\right) \tag{1}$$

where b is the reflected sky brightness, f is the incident solar radiation, R_1 and R_2 are reflection coefficients at the top and bottom of the water column, and q is the absorptive loss per pass through the water column. Of these parameters, the only one which conveys information about water depth is q, which is given by

$$q^2 = \frac{F-b}{R_2}\left(\frac{1}{(F-b)R_1 + f(1-R_1)^2}\right) \tag{2}$$

For a given absorption length τ, the water depth estimate is

$$d = -\frac{\tau}{2}\log[q^2] = -\tau\log[q] \tag{3}$$

If all of the relevant parameters (f, b, R_1, R_2, τ) were known, it would be a simple matter to convert an observed brightness F into an estimate of water depth d. However, none of these parameters are known with great precision, and some are only rather poorly known. Our strategy is to apply various constraints to the problem, and derive a self-consistent set of parameters.

One of the easiest parameters to estimate is the air–water interface reflectivity. The reflective properties of a surface depend on several factors, including the incidence angle of the radiation field, the roughness of the surface, and the optical properties of the materials on both sides of the interface. For nearly normal incidence angles, the optical reflectivity of a smooth interface depends rather simply on the change in the speed of light across the interface. The refractive index of a medium is just the value of

$$n = \frac{c}{v} \tag{4}$$

with c the speed of light in a vacuum, and v the phase speed of light within the medium. In terms of the refractive indices of the materials on either side of the interface, the Fresnel reflection

coefficient (reflectivity) at high incidence angles, for a smooth surface, is (Vidot & Santer, 2005; Walker, 1994)

$$R = \left(\frac{n_1 - n_2}{n_1 + n_2}\right). \tag{5}$$

The part of the incident beam which is not reflected is transmitted through the interface, and the corresponding transmission coefficient (transmissivity) is just the remainder:

$$T = 1 - R \tag{6}$$

Note that the values of reflection and transmission coefficients are the same for light incident on the interface from either side. They only depend on the absolute value of the difference in refractive index, not on the sign.

The real part of the refractive index of water is close to 4/3. The corresponding air–water interface reflectivity is 1/49, or roughly 2%. It has a relatively weak dependence on wavelength, particularly when compared to the large variations in the imaginary part, and also a weak dependence on salinity (Maykut & Light, 1995; Smith & Baker, 1981). This latter property is the physical basis of refractometers which are used in industrial and commercial
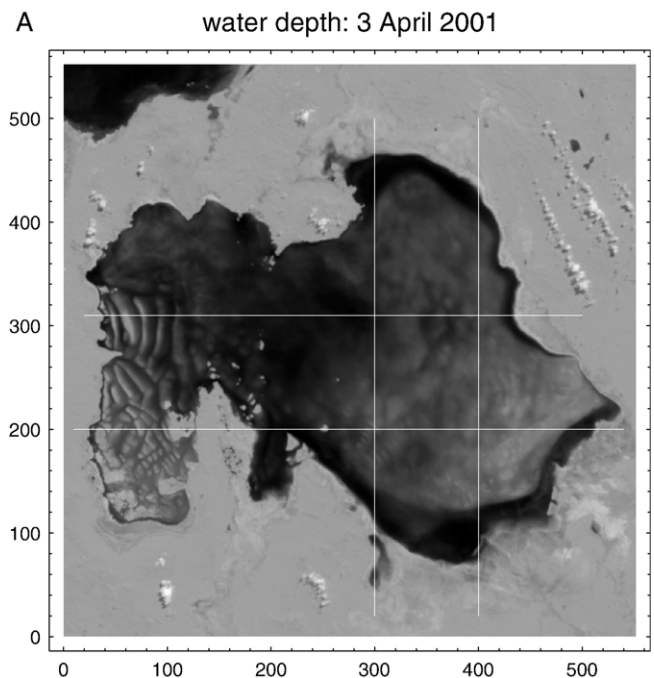

Fig. 8. Water depth estimate for 3 April 2001. A) The spatial pattern of estimated water depth variations across the Salar de Uyuni on 3 April 2001 is depicted as salt surface topography variations. The tick marks indicate location, in terms of the number of 275 m pixels from the SE corner. The white lines indicate locations of profiles. B) East–west profiles. The northern profile (row 200) clearly shows the peripheral moat on the eastern edge (near column 500), an essentially linear deepening to the west (200–460), interrupted by a small island (250). The western arm of the salar (20–100) is shallower and more irregular than the larger eastern arm. The southern profile shows a narrower peripheral moat on the east edge (430), a gradual deepening to the west (180–420), and a very pronounced series of ridges on the western margin (40–170). C) North–south profiles. Both of these profiles indicate pronounced peripheral moats at the northern and southern extremities of the salar.
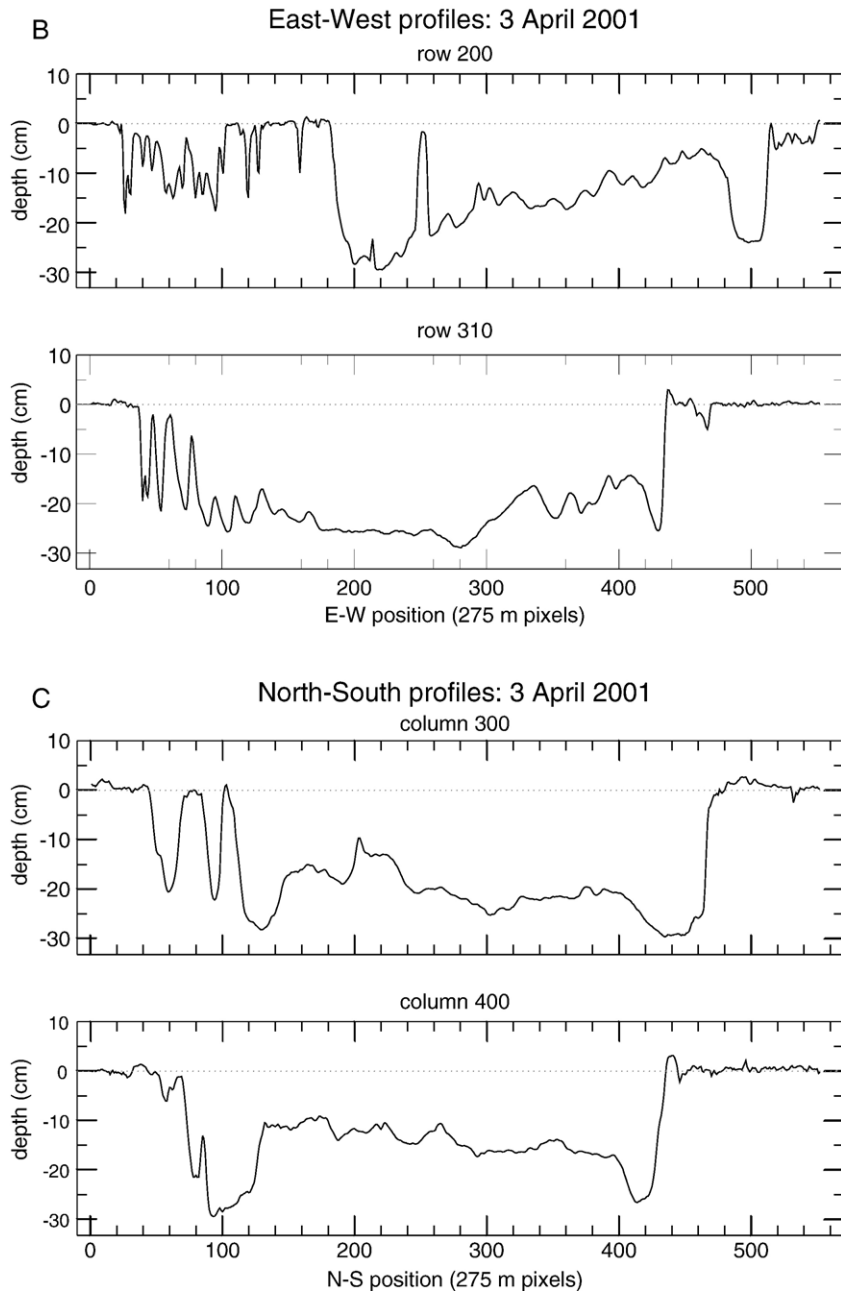
Fig. 8 (*continued*).

applications where control of salinity in brines is important. However, the variation in reflectivity at an air–water interface between pure water and a saturated brine is small, and will be ignored.

Given that the air–water interface reflectivity R_1 is small, we can obtain an approximate expression for the absorptive loss by simply setting this reflectivity to zero. The resulting estimate is

$$q^2 = \frac{F-b}{fR_2} \qquad (7)$$

Note that this is formally inconsistent, in that the sky brightness term b is strongly dependent upon reflection at the

air–water interface. However, as a practical matter, we will consider them to be independent quantities.

As the incident radiation f depends on the distance, intrinsic brightness, and elevation angle of the Sun, it can be readily computed. One advantage of using MISR data for our analysis is that this quantity is available as a standard data product. Using this information, and the observed brightness of the salt surface in the dry images, we can easily determine the reflectivity of the salt at each location and each relevant wavelength band.

Though we can directly image the salt–air interface, it is not quite obvious how to convert that observation into an estimate of the salt–water interface reflectivity. We note that the salt surface appears very bright, and is very nearly a Lambertian reflector.

The tabulated refractive index of halite is $n = 1.544$. If the salt layer were a single large crystal, the reflection coefficient would be small almost as small as when water covers the surface. Pure crystalline halite is noted for low optical absorption in the infrared, and has been used as a window material for lasers (Nistor et al., 1989). However, the optical behavior of a water-saturated aggregate of small crystals is expected to be quite different from that of the constituents (Nayar et al., 1991), and remote sensing observations of evaporite surfaces present challenges for mineralogical interpretation (Chapman et al., 1989; Drake et al., 1995; Howari et al., 2002).

We assume that the reflectivity variations, which are seen in images of the dry salt surface, are due to varying amounts of silicate dust, and that they are also manifest in the spatial variations in the salt–water interface reflectivity. For lack of an adequate physical model of the process, we simply assume that the wet and dry reflectivities are linearly related,

$$R_{\text{wet}} = \gamma R_{\text{dry}} \tag{8}$$

with γ representing an empirically derived scale factor, which may be different in each wavelength band, but is assumed not to depend on time.

Though we have listed laboratory derived estimates of the absorption lengths in pure water, at each of the 4 MISR wavelength bands, these values may not be applicable. They were obtained for pure water, and the water which covers the salt layer deviates from that ideal in several ways. At a minimum, it contains significant amounts of dissolved salt, and may also have some wind transported dust in suspension, as well.

Due to the complexity of the situation, we do not simply apply the algorithm above with laboratory derived-parameter estimates. Instead, we use independent estimates of salt surface topography, over selected profiles of the Salar de Uyuni, and calibrate our model to those estimates. Once we have obtained appropriate parameter values, we then use the model to map water depth variations over the entire surface.

4. Application

In this section, we describe the data used, and our application of the algorithm described above. We first briefly describe the criteria used to select data, and then list the particular scenes we have actually analyzed. We also list the steps in our analysis.

4.1. Instrumental background

The MISR instrument (Bruegge et al., 2002; Diner et al., 1998) is one of several on the Terra spacecraft, a component of the NASA Earth Observing System. It was launched on 18 December 1999 into in a nearly circular, high inclination ($I = 98.3°$), sun-synchronous orbit at mean elevation of 705 km. The orbital period and inclination conspire to yield a 16 day repeat track comprised of 233 separate orbits, and the fields of view of the cameras are wide enough to provide nearly global coverage every 9 days. We have only used data collected when the ground track passed close to the center of our area of interest, which encompasses blocks 106 and 107 within World Reference System-2 path 233.

As mentioned above, there are 4 spectral bands, and 9 separate cameras: one nadir-directed, and 4 each pointing fore and aft, with inclinations of 26.1°, 45.6°, 60.0°, and 70.5°. In Local Mode, the image resolution is 275 m in the cross-track direction, and the nadir camera yields the same resolution in the along track direction. In Global Mode, the individual pixels are averaged (4×4, 1×4, or 2×2) before transmission to the ground. All of our analyses were restricted to nadir camera images, with 275×275 m pixels.

In this study we use the level 1B2 terrain-projected radiance product (Lewicki et al., 2003). The level 1B2 geo-rectified radiance products are obtained by first projecting the top of the atmosphere radiance to the reference ellipsoid using spacecraft supplied pointing, and position information. This array is then projected onto a topographic surface. We also use MISR geometric, and geographic products (Lewicki et al., 2003), which provide information on solar position and view angles, and latitude and longitude information within each block.

4.2. Wet and dry images

Each year the Altiplano experiences some rain during the austral summer, but the amount of rain varies substantially from year to year. The wettest period of time on the Altiplano since the launch of Terra in late 1999 was the austral summer of October 2000 to March 2001. We examined all of the MISR
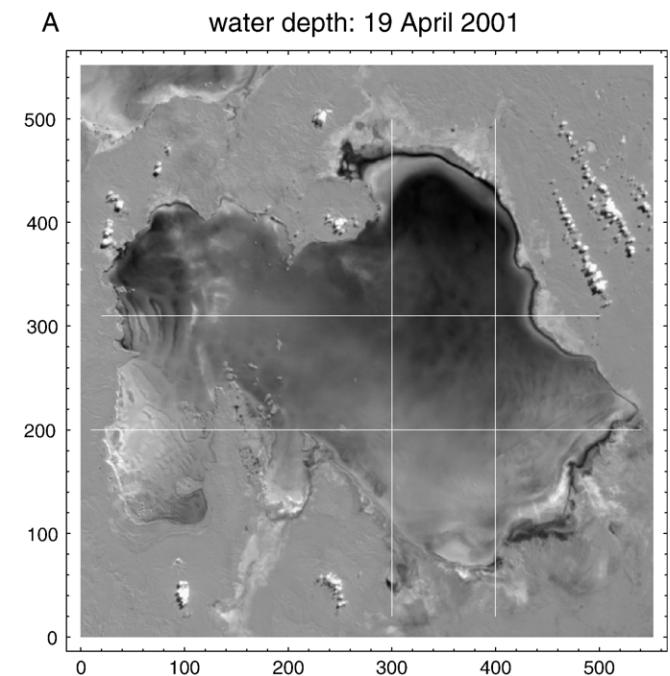

Fig. 9. Water depth estimate for 19 April 2001. A) Spatial pattern, with same format as Fig. 8A. The basic pattern of features is similar on the two dates. The primary difference, as is seen more clearly in Fig. 10, is a net decrease in water level on the later date, and a transfer of water from south to north. B) East–west profiles, same format as Fig. 8B. There is very little difference between the two dates on the southern profile, but the northern profile shows a deepening of the water. C) North–south profiles, same format as Fig. 8C.
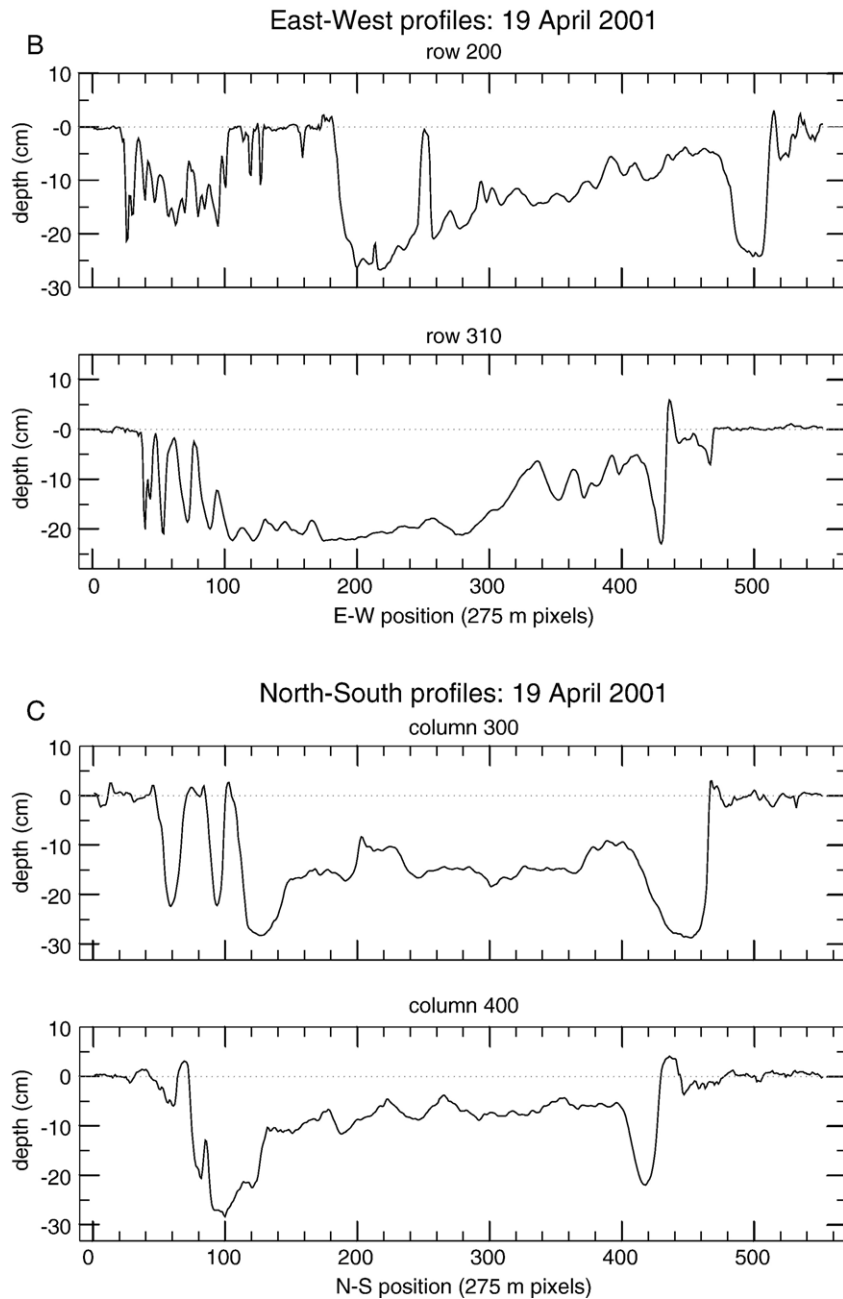
Fig. 9 (*continued*).

images acquired in our study area between 3 April and 26 September 2001. The early April image was the first of the sequence in which the cloud cover was essentially gone. At that time, all of the salt was covered by water. By mid-June most of the water on the salar had evaporated.

For our dry salt images, we used an image acquired on 18 October 2003. This is late in the dry season of a relatively dry year. By early May of 2003, the images showed relatively little water on the surface, though there was substantial water at that time of year in 2001. Fig. 4 compares the study area, as seen by MISR, at dry and wet times. When the salt surface is dry, it is much brighter than the surrounding area, but when it is covered by even a few cm of water, it is much darker than the sur-

rounding area. Though it is difficult to see in an image with large dynamic range, the dry salt surface does have subtle, but systematic, variations in brightness. While we can approximate the reflective loss at the air–water interface as a constant fraction of the incident radiation, treating the reflection from the water–salt interface as spatially constant would introduce systematic errors in our water depth estimates. We note that the general pattern of variation seen in the salt surface reflectivity is such that regions which are lower in elevation are darker. If we ignored this effect, we would over-estimate the amount of absorption required to yield the observed brightness at those locations, and would thus over-estimate the depth at the lowest points.

As will be shown below, the elevation difference between the highest and lowest points on the salt surface is well below 1 m. It thus seems unlikely that aeolian processes contribute directly to this subtle variation. When we first saw this effect, in the June and July images of 2001, we were concerned that it indicated persistence of residual brine, above the solid salt, in these lowest portions of the surface. That was part of our motivation for examining images from November 2003. The fact that the surface appears very similar at both of those times suggests that residual brine is not the explanation. A hypothesis we favor, but have not been able to either confirm or refute, is that the slight darkening of the "valleys" is due to deposition of silicate dust from the surrounding area, which would have been transported there either in suspension in the water flowing onto the salar from surrounding areas, or by wind blowing onto the surface of the temporary lake. If that is correct, we expect that the dust is cemented into the salt, and is not easily removed by subsequent wind.

4.3. Processing

The first step in preparing the images for water depth estimation is to visually examine each band. The selected time frame of our images was largely dictated by a desire to have little or no cloud cover present. On some of the images, there are a few pixels with missing values. For isolated errors of this type, the values were interpolated from adjacent values.

The second step was to correct for variations in illumination geometry. The ancillary information provided in the Geometric Parameters files includes solar zenith angle at each location within the image. Dividing by the cosine of this angle makes the images taken at different times of year more nearly comparable.

The third step is to divide by the solar irradiance, averaged over each MISR band. This yields an effective land surface reflectance or albedo at each pixel (Fang et al., 2004; Liang, 2001). The dry image values are then used to estimate a local effective salt–air reflectance. We use these values, and a constant scale factor to estimate the local salt–water reflectance values. These are then combined with the corresponding wet image surface reflectance values, and the air–water interface reflectance, to estimate the absorption per pass through the water column.

In the last step of the analysis, the water column depth is estimated from the Lambert–Beer law. This requires, as input, the inferred absorption from the wet and dry images, and the calibration-derived values for absorptivity.

4.4. Calibration

In order to estimate the empirical parameters in our water depth model, we use salt surface topography estimates along selected profiles, and adjust the model parameters to optimize agreement between model and observations. For this purpose, we use topography measurements obtained from an orbiting laser altimeter; the Geoscience Laser Altimeter System (GLAS), on the ICESat satellite (Abshire et al., 2005; Zwally et al., 2002). The Salar de Uyuni, due to its optical and topographic

similarity to polar ice fields, has been identified as a calibration target for ICESat. A GPS survey of a 54×45 km section of the salar surface was completed in September 2002 (Fricker et al., 2005). Since that time, many passes of ICESat data have been collected across the Salar de Uyuni, both within the GPS survey grid, and farther west.

Fig. 5 illustrates the location of the GPS survey, and ICESat track number 1320. In a typical ICESat elevation profile, the standard deviation of the difference between the GPS and GLAS estimates is 3–4 cm. We use a single ICESat track to calibrate our MISR-derived depth model, and then compare the depth estimates with topography in the GPS survey area.

We note that the GPS and ICESat measurements yield, in a relatively direct way, estimates of the positions of surface points in the WGS84 reference frame. In contrast, the passive optical estimates relate directly to water depth, and only rather indirectly to salt surface height. If wind and tidal perturbations can be ignored, the water surface will coincide with an equipotential surface. However, as will be seen below, there are long wavelength variations in inferred water depth between 3 and 19 April, 2001, which are likely due to wind or tidal variations.

In addition, the height of the geoid, which is the gravitational equipotential surface roughly coincident with mean global sea level, is not known with centimeter-level accuracy in the central Andes, nor over much of the land surface of the Earth (Kern et al., 2003; Schrama, 2003). Using a combination of global geoid models for the long wavelength component (Lemoine et al., 1998), and calculations based on an extensive surface gravimetric data base (Cady & Wise, 1992), it is possible to construct a local quasi-geoid with sufficient accuracy (Borsa, 2005).
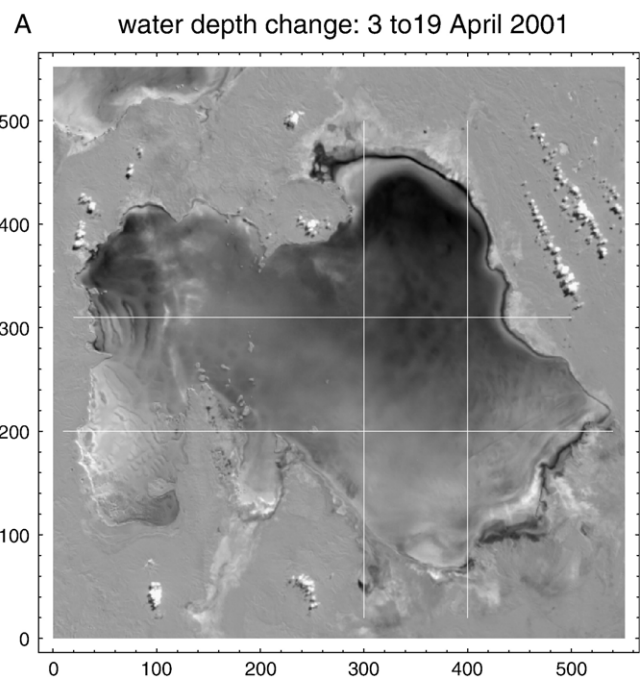

Fig. 10. difference in water depth estimates between 3 and 19 April 2001. A) Spatial pattern. The main feature visible is a transfer of water from south to north. Less evident visually, but still significant, is a net decline in water level due to evaporation. B) East–west profiles. C) North–south profiles.
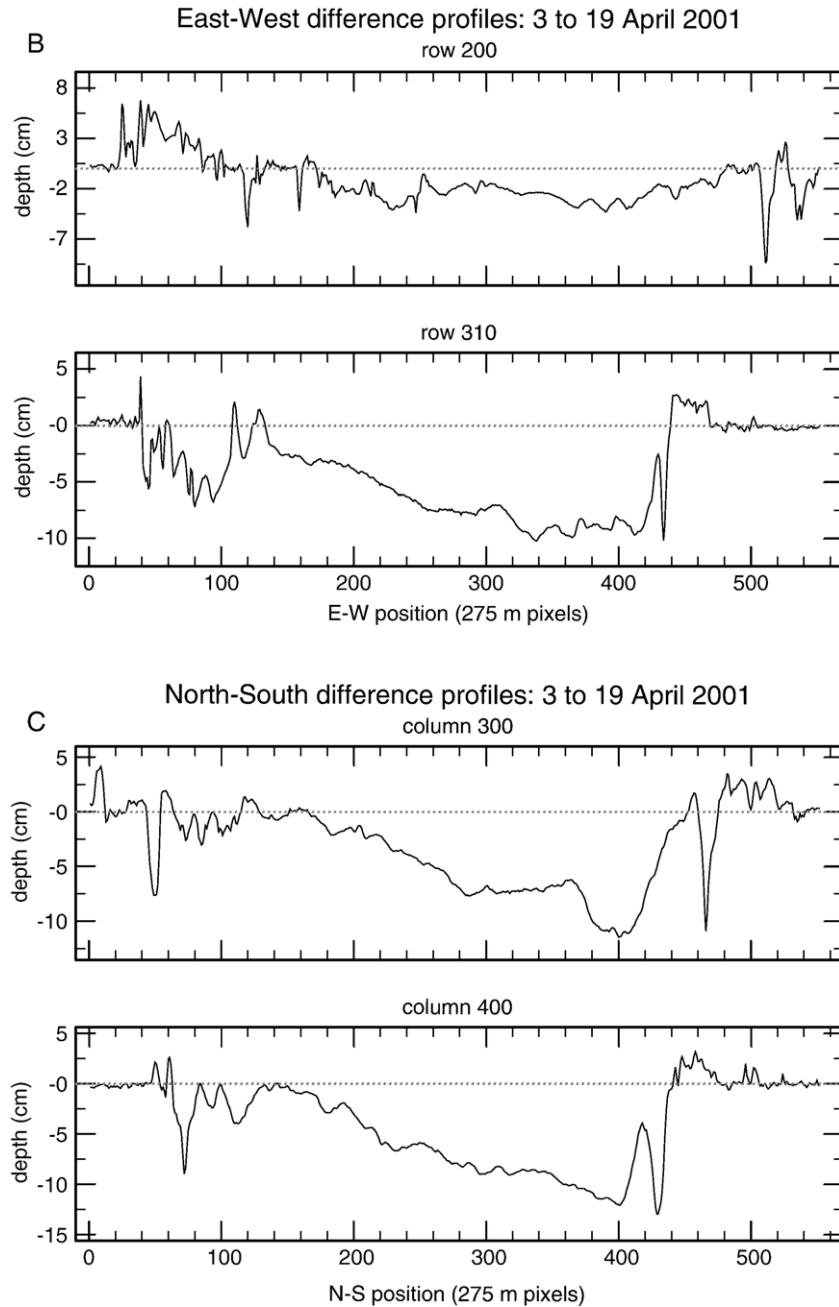
Fig. 10 (*continued*).

For our comparison between the MISR and ICESat results, we can take a much more direct route. That is, we can simply remove long wavelength features from both of the surfaces, and then compare the filtered water depth with the filtered ICESat profiles. ICESat measures the average elevation within a 70 m diameter spot, 40 times per second. This yields along-track spacing of 170 m. The MISR-derived estimates were evaluated at the locations of the ICESat elevation measurements. For each profile, a quadratic function in along-track distance was fit to the elevations and removed. The ICESat data were also slightly smoothed, via convolution with a Dirichlet kernel with half-width 5 times the point-to-point spacing.

For each of the 4 spectral bands of MISR, we used the data from 19 April 2001 and estimated the parameters of our depth model which yield the best agreement with the 70 km long GLAS elevation profile from track 1320. We selected that track because it has more relief on it than is seen in the tracks farther east. Fig. 6 illustrates the resulting salt surface topography estimates for each spectral band, compared to the GLAS profile. Fig. 7 shows scatter plots of the GLAS-derived estimates against the MISR-derived estimates, for each spectral band. As anticipated, the infrared channel performed best.

For each spectral band, we estimated 3 parameters: the sky brightness, the absorption length, and the ratio of wet and dry

salt surface reflectivities. The estimates were obtained via a least-squares adjustment of the MISR-derived elevation profile to the GLAS-derived elevation profile. The inferred values of absorption length were {21.5, 143, 145, 149} cm, for the infrared, red, green, and blue channels, respectively. The infrared value is quite close to the value listed in Table 1, based on laboratory estimates. The values for the other bands are much shorter than the pure-water laboratory estimates. This might reflect substantial increases in absorption, compared to pure water, or might simply reflect the poor performance, in these spectral bands, of the water depth estimation algorithm, due to the very shallow water. A better approach, but one we have not pursued at present, would use all four spectral bands, and all 9 viewing angles, to derived improved estimates of the relevant parameters.

The standard deviation of the difference between the MISR-derived elevation estimates and the ICESat-derived values to which the model was calibrated was 6.1 cm. The standard deviation of the difference between MISR-derived estimates and the GPS values in the survey area was 2.4 cm. It should be noted that the salt surface in the GPS survey area is considerably smoother than along the ICESat track used for calibration.

5. Results

In this section, we present the results of our analysis, using the parameters inferred from the ICESat profiles, and applied to MISR images taken on two dates in April of 200, when there was complete water coverage of the salar.

Figs. 8 and 9 illustrate the water depth variations derived from the 3 and 19 April 2001 infrared MISR data, using the 18 October 2003 image for the dry salt surface, and parameter values derived from the fit to the GLAS data. In both figures, we present water depth variations with the sign reversed, as though they were topographic variations on the salt surface. Fig. 10 illustrates the difference in our estimates of water depth between 3 and 19 April 2001. Rather than mask out the non-salar surface, we show it to give an indication of the random and systematic errors in our algorithm. If there were no errors, the regions away from the salt surface should be completely featureless. Some differences between the two wet-scene times, such as clouds (present on 3 April, but not on 19 April), are quite evident, but of no real consequence. Other differences, such as evaporative loss of water and wind-driven motion of the water across the surface are more significant.

Several features of the results of this analysis deserve attention. First is that the water depth, and implied salt surface elevation, are very uniform. There is substantially less than 1 m of relief on the salt surface. The largest feature seen in the surface topography is a slightly lower elevation around most of the margin of the salt. This peripheral moat is widest and deepest at the points on the periphery where ephemeral streams flow onto the salt during the rainy season. We infer that the relatively fresh water brought by these streams dissolves some of the salt in the crust and redeposits it further toward the center of the basin.

The second type of topographic feature we note is a series of equally spaced, parallel ridges. The most pronounced example

is near the western margin. Smaller sets of similar ridges are also seen near the center of the image, just east of the peninsula which nearly divides the salar into eastern and western portions. The processes responsible for forming these ridges are not presently understood. We do not know the age of these features, other than that they post-date the formation of the surface, and that they are clearly visible, in essentially their present configuration in LandSat images from March 1973 and June 1975.

Among the hypotheses we have considered are endogenic processes, such as salt diapirism (Ge et al., 1997; Hughes & Davison, 1993), and more surficial processes associated with water transport of salt in solution. Several observations seem to support the surficial transport hypotheses, including the north–south alignment of the ridge crests, and the proximity of the main ridge groups to low points on adjacent mountain fronts, allowing winds to drive waves in the water.

When the salar is flooded to a depth of 30–50 cm, as in 2001, the period of the main seiche mode of the lake is close to 12 hours, which makes it susceptible to resonant forcing by either semi-diurnal tides (Elliott et al., 2003), atmospheric pressure variations (Gomis et al., 1993; Vilibic et al., 2004) or winds (Luettich et al., 2002; Monserrat et al., 1998; Vilibic et al., 2005). There are quite significant diurnal and semi-diurnal winds on the Altiplano, both those associated with the South American low level jet (Bonner, 1968; Falvey & Garreaud, 2005; Garreaud & Wallace, 1997), and those driven locally (Egger et al., 2005). It is tempting to suppose that these ridges in the salt surface are somehow analogous to tidal sand bars in shallow marine environments (Hulsher, 1996; Hulsher et al., 1993; Roos et al., 2004), though the details of the formation process surely differ.

6. Summary

We have developed a simple algorithm for estimating water depth from passive optical observations, and applied it in a nearly ideal setting. The water on the surface of the Salar de Uyuni in April 2001 varied only slightly in depth over the 100 × 100 km extent of the salt surface, and varied even less between the dates of 3 and 19 April. This basic approach could be easily adapted to routine observations of water depth in shallow lacustrine and marine environments worldwide. The achievable accuracy in relatively clear and shallow water is at the level of a few centimeters. If the multi-angle data of MISR were fully exploited, it would be possible to extend the approach into less ideal circumstances, with suspended sediments or other sources of scattering in the water column.

This approach also permits evaluation of extremely subtle topographic features on low relief surfaces. We have demonstrated that the salt surface at Salar de Uyuni, despite being extremely flat, is not completely devoid of topographic features. There are essentially linear, low-lying troughs around most of the perimeter, roughly equant mounds over much of the surface, and pronounced sets of oriented ridges in select locations. However, all of these features are small enough in vertical extent, and large enough in horizontal extent, to be quite invisible from eye-level, when standing on the surface. An area

of future research which this technique enables is the exploration of topography and geomorphic processes on surfaces sufficiently flat, level, and smooth that they have heretofore been seen as the asymptotic end-state of planation or erosional processes. We expect that this new field of crypto-geomorphology will provide insights into the more prosaic realm of traditional scale geomorphologic features and procesess.

References

Abbott, M. B., Binford, M. W., Brenner, M., & Kelts, K. R. (1997). A 3500 C–14 yr high resolution record of water level changes in Lake Titicaca. *Quaternary Research*, *47*, 169−180.

Abshire, J. B., Sun, X. L., Riris, H., Sirota, J. M., McGarry, J. F., Palm, S., et al. (2005). Geoscience Laser Altimeter System (GLAS) on the ICESat mission: On-orbit measurement performance. *Geophysical Research Letters*, *32*, L21S02.

Adler-Golden, S. M., Acharya, P. K., Berk, A., Mathew, M. W., & Gorodtzky, D. (2005). Remote bathymetry of the littoral zone from AVIRIS, LASH and QuickBird imagery. *IEEE Transactions on Geoscience and Remote Sensing*, *43*, 337−347.

Agassiz, A. (1876). Hydrographic sketch of Lake Titicaca. *Proceedings of the American Academy of Arts and Sciences*, *11*, 283−305.

Argollo, J., & Mourguiart, P. (2000). Late Quaternary climate history of the Bolivian Altiplano. *Quaternary International*, *72*, 37−51.

Baker, P. A., Rigsby, C. A., Seltzer, G. O., Fritz, S. C., Lownstein, T. K., Bacher, N. P., et al. (2001a). Tropical climate changes at millenial and orbital timescales on the Bolivian Altiplano. *Nature*, *409*, 698−701.

Baker, P. A., Seltzer, G. O., Fritz, S. C., Dunbar, R. B., Grove, M. J., Tapia, P. M., et al. (2001b). The history of South American tropical precipitation for the past 25,000 years. *Science*, *291*, 640−643.

Baucom, P. C., & Rigsby, C. A. (1999). Climate and lake level history of the northern Altiplano, Bolivia, as recorded in Holocene sediments of the Rio Desaguadero. *Journal of Sedimentary Research*, *69*, 597−611.

Benson, L. (1994). Carbonate deposition, Pyramid Lake subbasin, Nevada 1. Sequence formation and elevational distribution of carbonate deposits. *Palaeogeography, Palaeoclimatology, Palaeoecology*, *109*, 55−87.

Bierwirth, P. N., Lee, T. J., & Burne, R. V. (1993). Shallow sea-floor reflectance and water depth derived by unmixing multispectral imagery. *Photogrammetric Engineering and Remote Sensing*, *59*, 331338.

Bills, B. G., de Silva, S. L., Currey, D. R., Emenger, R. S., Lillquist, K. D., Donnellan, A., et al. (1994). Hydro-isostatic deflection and tectonic tilting in the Central Andes: Initial results of a GPS survey of Lake Minchin shorelines. *Geophysical Research Letters*, *21*, 293−296.

Bobst, A. L., Lowenstein, T. K., Jordan, T. E., Godfrey, L. V., Ku, T. L., & Luo, S. D. (2001). A 106-ka paleoclimate record from drill core of the Salar de Atacama, northern Chile. *Palaeogeography, Palaeoclimatology, Palaeoecology*, *173*, 21−42.

Bonner, W. D. (1968). Climatology of the low-level jet. *Journal of Applied Metalworking*, *3*, 339−347.

Borsa, A. A. Geomorphology of the Salar de Uyuni, Bolvia, Ph.D. dissertation, University of California, San Diego, 2005.

Bowman, I. (1909). The physiography of the central Andes. *American Journal of Science*, *28*, 373−402.

Bruegge, C. J., Chrien, N. L., Ando, R. R., Diner, D. J., Abdou, W. A., Helmlinger, M. C., et al. (2002). Early validation of the Multi-angle Imaging Spectro-Radiometer (MISR) radiometric scale. *IEEE Transactions on Geoscience and Remote Sensing*, *40*, 1477−1492.

Bryant, R. G. (1999). Application of AVHRR to monitoring a climatically sensitive playa. Chott el Djerid, southern Tunisia. *Earth Surface Processes and Landforms*, *24*, 283−302.

Cady, J. W., & Wise, R. A. (1992). Gravity and magnetic studies. *Geology and mineral resources of the Altiplano and Cordillera Occidental, Bolvia, U.S Geological Survey Bulletin 1975* (pp. 56−61).

Castaneda, C., Herrero, J., & Casterad, M. A. (2005). Landsat monitoring of playa-lakes in the Spanish Monegros desert. *Journal of Arid Environments*, *63*, 497−516.

Chapman, J. E., Rothery, D. A., Francis, P. W., & Pontual, A. (1989). Remote sensing of evaporite mineral zonation in salt flats (salars). *International Journal of Remote Sensing*, *10*, 245−255.

Chepstow-Lusty, A., Bush, M. B., Frogley, M. R., Baker, P. A., Fritz, S. C., & Aronson, J. (2005). Vegetation and climate change on the Bolivian Altiplano between 108,000 and 18,000 yr ago. *Quaternary Research*, *63*, 90−98.

Clark, R. K. (1987). Bathymetry calculations with Landsat 4 TM imagery. *Applied Optics*, *26*, 4036−4038.

Cross, S. L., Baker, P. A., Seltzer, G. O., Fritz, S. C., & Dunbar, R. B. (2000). A new estimate of the Holocene lowstand of Lake Titicaca, central Andes, and implications for tropical paleohydrology. *Holocene*, *10*, 21−32.

Currey, D. R. (1994a). Hemiarid lake basins: hydrographic patterns. In A. D. Abrahams & A. J. Parsons (Eds.), *Geomorphology of desert environments* (pp. 405−421). Chapman and Hall.

Currey, D. R. (1994b). Hemiarid lake basins: Geomorphic patterns. In A. D. Abrahams & A. J. Parsons (Eds.), *Geomorphology of desert environments* (pp. 422−444). Chapman and Hall.

Diner, D. J., Beckert, J. C., Reilly, T. H., Bruegge, C. J., Conel, J. E., Kahn, R. A., et al. (1998). Multi-angle Imaging SpectroRadiometer (MISR): Instrument description and experiment overview. *IEEE Transactions on Geoscience and Remote Sensing*, *36*, 1072−1087.

Drake, N. A. (1995). Reflectance spectra of evaporite minerals (400–2500 nm): Applications for remote sensing. *International Journal of Remote Sensing*, *16*, 2555−2571.

Egger, J., Blacutt, L., Ghezzi, F., Heinrich, R., Kolb, P., Lammlein, S., et al. (2005). Diurnal circulation of the Bolivian Alitplano, part I, observations. *Monthly Weather Review*, *133*, 911−924.

Elliott, A. J., Ellis, K. M., & Lynn, N. M. (2003). Baroclinic tidal currents in the Gareloch, Scotland. *Estuarine, Coastal and Shelf Science*, *58*, 107−116.

Falvey, M., & Garreaud, R. D. (2005). Moisture variability over the South American Altiplano during the South American low level jet experiment (SALLJEX) observing season. *Journal of Geophysical Research*, *110* Art. No. D22105.

Fang, H., Liang, S., Chen, M., Walthall, C., & Daughtry, C. (2004). Statistical comparisons of MISR, ETM, and MODIS land surface reflectance and albedo products of the BARC land validation core site. *International Journal of Remote Sensing*, *25*, 409−422.

Felton, A., Jewell, P. W., Chan, M., & Currey, D. (2006). Controls of tufa development in Pleistocene Lake Bonneville, Utah. *Journal of Geology*, *114*, 377−389.

Finkl, C. W., Benedet, L., & Andrews, J. L. (2005). Interpretation of seabed geomorphology based on spatial analysis of high density airborne laser bathymetry. *Journal of Coastal Research*, *21*, 501−514.

Fonstad, M. A., & Marcus, W. A. (2005). Remote sensing of stream depths with hydraulically assisted bathymetry models. *Geomorphology*, *72*, 320−339.

Ford, T. D., & Pedley, H. M. (1996). A review of tufa and travertine deposits of the world. *Earth Science Reviews*, *41*, 117−175.

Fornari, M., Risacher, F., & Feraud, G. (2001). Dating of paleolakes in the central Altiplano of Bolivia. *Palaeogeography, Palaeoclimatology, Palaeoecology*, *172*, 269−282.

Fricker, H. A., Borsa, A., Minster, B., Carabajal, C., Quinn, K., & Bills, B. (2005). Assessment of ICESat performance at the Salar de Uyuni, Bolivia. *Geophysical Research Letters*, *32*, L21S06.

Garreaud, R. D., & Aceituno, P. (2001). Interannual rainfall variability over the South American Altiplano. *Journal of Climate*, *14*, 2779−2789.

Garreaud, R. D., & Wallace, J. M. (1997). The diurnal march of convective cloudiness over the Americas. *Monthly Weather Review*, *125*, 3157−3171.

Ge, H., Jackson, M. P. A., & Vendeville, B. C. (1997). Kinematics and dynamics of salt tectonics driven by progradation. *AAPG Bulletin*, *81*, 398−423.

Gomis, D., Monserrat, S., & Tintore, J. (1993). Pressure forced seiches of large amplitude in inlets of the Balearic islands. *Journal of Geophysical Research*, *98*, 14437−14445.

Gordon, H. R. (1989). Can the Lambert–Beer law be applied to the diffuse attenuation coefficient of ocean water? *Limnology and Oceanography*, *34*, 1389−1409.

Gordon, H. R., Brown, O. B., & Jacobs, M. M. (1975). Computed relationships between inherent and apparent optical properties of a flat homogeneous ocean. *Applied Optics*, *14*, 417−427.

Guenther, G. C., Brooks, M. W., & LaRocque, P. E. (2000). New capabilities of the "SHOALS" airborne lidary bathymeter. *Remote Sensing of Environment*, *73*, 247−255.

Hale, G. M., & Querry, M. R. (1973). Optical constants of water in the 200 nm to 200 μm wavelength region. *Applied Optics*, *12*, 555−563.

Hart, W. S., Quade, J., Madsen, D. B., Kaufman, D. S., & Oviatt, C. G. (2004). The Sr^{87}/Sr^{86} ratios of lacustrine carbonates and lake-level history of the Bonneville paleolake system. *Geological Society of America Bulletin*, *116*, 1107−1119.

Howari, F. M., Goodell, P. C., & Miyamoto, S. (2002). Spectral properties of salt crusts formed on saline soils. *Journal of Environmental Quality*, *31*, 1453−1461.

Hughes, M., & Davison, I. (1993). Geometry and growth kinematics of salt pillows in the southern North Sea. *Teconophysics*, *228*, 239−254.

Hulsher, S. J. M. H. (1996). Tidal-induced large scale regular bed form patterns in a three dimensional shallow water model. *Journal of Geophysical Research*, *101*, 20727−20744.

Hulsher, S. J. M. H., Deswart, H. E., & Devriend, H. J. (1993). The generation of offshore tidal sand banks and sand waves. *Continental Shelf Research*, *13*, 1183−1204.

Isoun, E. C., Fletcher, N., & Frazer, J. (2003). Multi-spectral mapping of reef bathymetry and coral cover, Kailua bay, Hawaii. *Coral Reefs*, *22*, 68−82.

Jordan, T. E., Munoz, N., Hein, M., Lowenstein, T., Godfrey, L., & Yu, J. (2002). Active faulting and folding without topographic expression in an evaporite basin, Chile. *Geological Society of America Bulletin*, *114*, 1406−1421.

Kempf, S. K., & Tyler, S. W. (2006). Spatial characterization of land surface energy fluxes and uncertainty estimation at the Salar de Atacama, Northern Chile. *Advances in Water Resources*, *29*, 336−354.

Kern, M., Schwarz, K. P., & Sneeuw, N. (2003). A study on the combination of satellite, airborne, and terrestrial gravity data. *Journal of Geodesy*, *77*, 217−225.

Lafon, V., Froidefond, J. M., Lahet, F., & Castaign, P. (2002). SPOT shallow water bathymetry of a moderately turbid tidal inlet based on field measurements. *Remote Sensing of Environment*, *81*, 136−148.

Lamparelli, R. A. C., Ponzoni, F. J., Zullo, J., Pellegrino, G. Q., & Arnaud, Y. (2003). Characterization of the Salar de Uyuni for in-orbit satellite calibration. *IEEE Transactions on Geoscience and Remote Sensing*, *41*, 1461−1468.

Lee, Z. P., Carder, K. L., Mobley, C. D., Steward, R. G., & Patch, J. S. (1998). Hyperspectral remote sensing for shallow waters. I. A semi-analytical model. *Applied Optics*, *37*, 6329−6338.

Lee, Z. P., Carder, K. L., Mobley, C. D., Steward, R. G., & Patch, J. S. (1999). Hyperspectral remote sensing for shallow waters. II. Deriving bottom depths and water properties by optimization. *Applied Optics*, *38*, 3831−3843.

Lemoine, F. G., Kenyon, S. C., Factor, J. K., Trimmer, R. G., Pavlis, N. K., Chinn, D. S., et al. (1998). The development of the joint NASA GSFC and NIMA geopotential model EGM96. *NASA TP* (pp. 206861).

Lenters, J. D., & Cook, K. H. (1997). On the origin of the Bolivian high and related circulation features of the South American climate. *Journal of the Atmospheric Sciences*, *54*, 656−677.

Lenters, J. D., & Cook, K. H. (1999). Summertime precipitation variability over South America: Role of the large-scale circulation. *Monthly Weather Review*, *127*, 409−431.

Lewicki, S., Moroney, C., Crean, K., Gluck, S., Miller, K., & Paradise, S. (2003). Multi-angle Imaging Spectro-Radiometer (MISR) data products specifications. *JPL*, D-13963.

Liang, S. (2001). Narrowband to broadband conversions of land surface albedo. *Remote Sensing of Environment*, *76*, 213−238.

Lowenstein, T. K., Hein, M. C., Bobst, A. L., Jordan, T. E., Ku, T. L., & Luo, S. (2003). An assesment of stratigraphic completeness in climate-sensitive closed-basin lake sediments: Salar de Atacama, Chile. *Journal of Sedimentary Research*, *73*, 91−104.

Luettich, R. A., Carr, S. D., Fulcher, C. W., & McNinch, J. E. (2002). Semi-diurnal seiching in a shallow micro-tidal lagoonal estuary. *Continental Shelf Research*, *22*, 1669−1681.

Lyzenga, D. R. (1978). Passive remote sensing techniques for mapping water depth and bottom features. *Applied Optics*, *17*, 379−383.

Maykut, G. A., & Light, B. (1995). Refractive index measurements in freezing sea ice and sodium chloride brines. *Applied Optics*, *34*, 950−961.

Millard, R. C., & Seaver, G. (1990). An index of refraction algorithm for seawater over temperature, pressure, salinity, and wavelength. *Deep Sea Research*, *37*, 1909−1926.

Minchin, J. B. (1882). Notes of a journey through part of the Andean table-land of Bolivia in 1882. *Proceedings of the Royal Geographical Society*, *4*, 671−676.

Mobley, C. D., Sundman, L. K., Davis, C. O., Bowles, J. H., Downes, T. V., Leathers, R. A., et al. (2005). Interpretation of hyperspectral remote-sensing imagery by spectrum matching and look-up tables. *Applied Optics*, *44*, 3576−3592.

Monserrat, S., Rabinovich, A. B., & Casas, B. (1998). On the reconstruction of the transfer function for atmospherically generated seiches. *Geophysical Research Letters*, *25*, 2197−2200.

Nayar, S. K., Ikeuchi, K., & Kanade, T. (1991). Surface reflection: Physical and geometrical perspectives. *IEEE Transactions on Pattern Analysis and Machine Intelligence*, *13*, 611−634.

Nelson, S. T., Wood, M. J., Mayo, A. L., Tingey, D. G., & Eggett, D. (2005). Shoreline tufa and tufaglomerate from Pleistocene Lake Bonneville, Utah: Stable isotopic and mineralogic records of lake conditions, processes, and climate. *Journal of Quaternary Science*, *20*, 3−19.

Nerem, R. S. (1990). Determination of the ocean circulation using GEOSAT altimetry. *Journal of Geophysical Research*, *95*, 3163−3175.

Nistor, S. V., Mateescu, C. D., Nistor, L. C., & Todorescu, V. S. (1989). Preparation and properties of ultra-transparent NaCl single crystals. *Crystal Research and Technology*, *24*, 525−529.

Philpot, W. D. (1989). Bathymetric mapping with passive multispectral imagery. *Applied Optics*, *28*, 1569−1578.

Placzek, C., Quade, J., & Patchett, P. J. (2006). Geochronology and stratigraphy of late Pleistocene lake cycles on the southern Bolivian Altiplano: Implications for causes of tropical climate change. *Geological Society of America Bulletin*, *118*, 515−532.

Ponzoni, F. J., Zullo, J., Lamparelli, R. A. C., Pellegrino, G. Q., & Arnaud, Y. (2004). In-flight absolute calibration of the LandSat-5 TM on the test site Salar de Uyuni. *IEEE Transactions on Geoscience and Remote Sensing*, *42*, 2761−2766.

Pope, R. M., & Fry, E. S. (1997). Absorption spectrum (380–700 nm) of pure water. *Applied Optics*, *36*, 8710−8723.

Rettig, S. L., Jones, B. F., & Risacher, F. (1980). Geochemical evolution of brines in the Salar de Uyuni, Bolivia. *Chemical Geology*, *30*, 57−79.

Risacher, F., & Fritz, B. (1991a). Quaternary geochemical evolution of the salars of Uyuni and Coipasa, Central Altiplano, Bolivia. *Chemical Geology*, *90*, 211−231.

Risacher, F., & Fritz, B. (1991b). Geochemistry of Bolivian salars, southern Altiplano: Origin of solutes and brine evolution. *Geochimica et Cosmochimica Acta*, *55*, 687−705.

Risacher, F., & Fritz, B. (2000). Bromine geochemistry of Salar de Uyuni and deeper crusts, central Altiplano, Bolivia. *Chemical Geology*, *167*, 373−392.

Risacher, F., Alonso, H., & Salazar, C. (2003). The origin of brines and salts in Chilean salars: A hydrochemical review. *Earth-Science Reviews*, *63*, 249−293.

Roche, M. A., Bourges, J., Cortes, J., & Mattos, R. (1992). Climatology and hydrology of the Lake Titicaca basin. In C. Dejoux & A. Iltis (Eds.), *Lake Titicaca* (pp. 63−88). Kluwer.

Roos, P. C., Hulscher, S. J. M. H., Knaapen, M. A. F., & Van Damme, R. M. J. (2004). The cross sectional shape of tidal sand banks: Modeling and observations. *Journal of Geophysical Research*, *109* Art. No. F02003.

Rosen, M. R. (1994). The importance of groundwater in playas: A review of playa classifications and the sedimentology and hydrology of playas. In M. R. Rosen (Ed.), *Paleoclimate and Basin Evolution of Playa Systems Geol. Soc. Amer. Spec. Paper, vol. 289.* (pp. 1−18).

Rouchy, J. M., Servant, M., Fournier, M., & Causse, C. (1996). Extensive carbonate algal bioherms in upper Pleistocene saline lakes of the central Altiplano of Bolivia. *Sedimentology*, *43*, 973−993.

Rowe, H. D., & Dunbar, R. B. (2004). Hydrologic energy balance constraints on the Holocene lake level history of lake Titicaca, South America. *Climate Dynamics*, *23*, 439−454.

Sandidge, J. C., & Holyer, R. J. (1998). Coastal bathymetry from hyperspectral observations of water radiance. *Remote Sensing of Environment, 65,* 341−352.

Schrama, E. J. O. (2003). Error characteristics estimated from CHAMP, GRACE and GOCE derived geoids and from satellite altimetry derived mean dynamic topography. *Space Science Reviews, 108,* 179−193.

Servant, M., & Fontes, J. C. (1978). Les lacs quaternaires des hauts plateaux de Andes Boliviennes. *Cah. ORSTOM, vol. 10.* (pp. 2−23).

Smith, R. C., & Baker, K. S. (1981). Optical properties of the clearest natural waters (200–800 nm). *Applied Optics, 20,* 177−184.

Sokoletsky, L. (2005). Comparative analysis of selected radiative transfer approaches for aquatic environments. *Applied Optics, 44,* 136−148.

Steinmann, G., Hok, H., & Bistram, A. (1904). Zur geolgie des suedestland Bolivien. *Zbl. Miner., vol. 5.* (pp. 1−4).

Stoertz, G. E., & Ericksen, G. E. (1974). Geology of salars in Northern Chile. *U.S. Geol. Surv. Prof. Paper, vol. 811.* (pp.) 65 pp.

Stumpf, R. P., Holderied, K., & Sinclair, M. (2003). Determination of water depth with high-resolution satellite imagery over variable bottom types. *Limnology and Oceanography, 48,* 547−556.

Vidot, J., & Santer, R. (2005). Atmospheric correction for inland waters — Application to SeaWiFS. *International Journal of Remote Sensing, 26,* 3663−3682.

Vilibic, I., Domijan, N., Orlic, M., Leder, N., & Pasaric, M. (2004). Resonant coupling of a traveling air pressure disturbance with the east Adriatic coastal waters. *Journal of Geophysical Research, 109* Art. No. C10001.

Vilibic, I., Domijan, N., & Cupic, S. (2005). Wind versus air pressure seiche triggering in the Middle Adriatic coastal waters. *Journal of Marine Systems, 57,* 189−200.

Yechieli, Y., & Wood, W. W. (2002). Hydrologic processes in saline systems: Plays, sabkhas, and saline lakes. *Earth Science Reviews, 58,* 343−365.

Yunus, W. M. M. (1992). Temperature dependence of refractive index and absorption of NaCl, $MgCl_2$, and Na_2SO_4 solutions as major components of natural seawater. *Applied Optics, 31,* 2963−2964.

Walker, R. E. (1994). *Marine light field statistics.* New York: John Wiley and Sons.

Wehrli, C. (1985). *Extraterrestrial solar spectrum, vol. 615.* W.R.C. Publication.

Wozencraft, J. M., & Lillycrop, W. J. (2003). SHOALS airborne coastal mapping: Past, present, and future. *Journal of Coastal Research, 38,* 207−215.

Zwally, H. J., Schutz, B., Abdalati, W., Abshire, J., Bentley, C., Brenner, A., et al. (2002). ICESat's laser measurements of polar ice, atmosphere, ocean, and land. *J. Geodyn., 34,* 405−445.